

Synoptic Lagrangian maps: Application to surface transport in Monterey Bay

by B. L. Lipphardt, Jr.^{1,2}, D. Small³, A. D. Kirwan, Jr.¹, S. Wiggins³, K. Ide⁴,
C E. Grosch⁵ and J. D. Paduan⁶

ABSTRACT

Here we report on an effort to describe in detail the evolution of surface water particles in Monterey Bay from the time they first enter until the time they leave. The data used for this study are objective mappings from hourly surface currents obtained from high frequency (HF) radar measurements in Monterey Bay for the period 2 June through 4 August 1999. The basic concept is simple: compute the origin and fate of a large number of particles for every hour during the analysis period. However, analyzing and displaying the enormous amount of computed trajectory information required a new data compression technique: synoptic Lagrangian maps produced by representing each trajectory by its origin/fate and its residence time. The results show unexpected complexity and variability not apparent in the Eulerian current archive. For example, the fraction of particles that escaped to the open ocean during this period varied from about 17 to more than 92 percent. Mean particle residence times ranged from 4.5 to 11 days. The distribution of particle residence times and transport pathways varied over time scales from hours to weeks, and space scales from 2 to 40 km. The wide range of variability in particle properties reported here shows that surface transport studies in Monterey Bay require detailed wind and tidal current information over the entire bay, as well as information about the flow along the open ocean boundary.

1. Introduction

Understanding the variability of surface transport and identifying the relative importance of transport pathways are important for addressing both practical problems as well as fundamental research questions in the coastal ocean. Most practical problems (oil spill risk assessment, harmful algal bloom studies, or search and rescue) focus on tracking the evolution of a small surface ocean “patch” near the coast. The origin of the particles making up the patch is of no concern in these cases, but their fate becomes critical. In contrast, many fundamental research problems addressing climate or ecological variability deal with a coastal region as an open system, where net particle transport is most relevant.

1. College of Marine Studies, University of Delaware, Newark, Delaware, 19716, U.S.A.

2. Corresponding author. *email: brucel@udel.edu*

3. School of Mathematics, University of Bristol, Bristol, United Kingdom.

4. Department of Atmospheric Sciences, University of California, Los Angeles, California, 90095, U.S.A.

5. Center for Coastal Physical Oceanography, Old Dominion University, Norfolk, Virginia, 23529, U.S.A.

6. Department of Oceanography, Naval Postgraduate School, Monterey, California, 93943, U.S.A.

In these cases, particle origin and fate, as well as residence time in the system, become important for assessing exchange between the coastal and open oceans.

Unfortunately it is prohibitively expensive to acquire sufficient Lagrangian observations to assess the origin, fate, and residence times of particles in coastal regions reliably. While trajectories can be computed from model velocities, computing enough trajectories for synoptic coverage adds a significant computational burden, so it is not routinely done. Here we compute trajectories directly from objective mappings of hourly synoptic Monterey Bay surface currents from HF radar. However, the approach can be applied to any Eulerian current archive and so has promise for wide application.

Our primary scientific interest is to identify transport pathways. Since this question is fundamentally Lagrangian in nature, we use Lagrangian trajectories from a grid of particles spaced uniformly at one-half km intervals over the bay's surface. Particles are tracked both backward and forward in time by integrating objectively analyzed surface currents from HF radar to determine their origin and fate. Several types of synoptic Lagrangian maps (SLMs) are constructed by color-coding each particle's initial position to represent information about its residence time and/or its origin/fate. SLMs that use only information from forward time integration are useful for addressing problems that focus only on particle fates. Combined information from backward and forward time particle integrations is used to identify transport pathways and determine total residence time. When the boundary is divided into open ocean and coastline segments, two cross-bay transport pathways (ocean to coast, and coast to ocean) and two recirculation pathways (ocean to ocean, and coast to coast) result.

CODAR-type HF radars measure only surface flow, so the surface layer is treated as two-dimensional, and our simulated particles are therefore buoyant. Many important problems related to larval transport, search and rescue, and hazardous spill mitigation, for example, are concerned with the movement of such buoyant particles. Our velocity mappings retain convergence and divergence structure (upwelling, for example) from the HF radar measurements, and the buoyant particles do converge and diverge in response to these processes. Our assumption of a two-dimensional surface flow is not a fundamental limitation, since the approach is readily extended to three dimensions when appropriate subsurface velocity information is available.

Here we analyze 62 days of hourly surface current maps for the period June-August 1999. Since we simulate buoyant surface particles, it is natural to consider the wind as one important possible forcing mechanism for surface transport. Summer winds in Monterey Bay are known to fluctuate between persistent periods (lasting several days) of upwelling-favorable conditions (winds blowing alongshore, directed to the southeast) interspersed with brief (2-3 day) relaxation events, when the wind veers to the left, typically blowing toward a direction between east and north (Rosenfeld *et al.*, 1994; Ramp *et al.*, 2005). Here, hourly wind measurements from Monterey Bay Aquarium Research Institute (MBARI) buoy M1, located near the center of Monterey Bay, are compared with some particle results to determine whether any relationship between winds and bulk particle

properties exists. Comparisons like these cannot conclusively demonstrate cause and effect relationships, however, since a single point measurement will not capture the spatial variability known to exist in the winds over Monterey Bay.

Other forcing mechanisms likely to be important are tidal currents and mesoscale surface current variability along the open boundary associated with the California Current system. Our velocity archive is too short to permit a tidal analysis that separates the influences of diurnal winds and tides. To consider influences from the California Current system, additional measurements outside our study area are required. Consequently, consideration of the impact of tides and offshore flow is deferred to future study.

The rest of this paper is organized as follows. The next two sections describe the SLM concept and the HF radar measurements. Section 4 describes the results obtained by application of the methodology to surface transport in Monterey Bay. The results are summarized and discussed in the last section. The Appendix gives a description of the objective mapping technique for HF radar current measurements.

2. Synoptic Lagrangian maps

a. The concept

Residence-time maps have been used in previous dynamical systems studies of systems that exhibit periodic variability (Meiss, 1997; Rom-Kedar *et al.*, 1990; Camassa and Wiggins, 1991). This approach has not previously been extended to nonstationary complex systems like Monterey Bay. Nevertheless the idea is attractive since it would provide a way of describing synoptic particle behavior.

We extend this dynamical systems approach in three important ways. First, the velocity field in Monterey Bay is nonstationary in the sense that there is no interval of time for which the velocity field is periodic. In this case, the map that describes particle motions changes from one measurement time to the next so that a single map cannot describe particle displacements. Second, for a synoptic grid of particles covering the entire bay, we track both the particle origin and fate by integrating both backward and forward in time until the particle encounters any boundary. This allows each particle's total residence time inside the bay to be specified. Third, we divide the domain boundary into segments, allowing each origin and escape event to be classified by its boundary location. When two boundary segments are used (the open ocean boundary and the coastline) four possible transport paths result: two "recirculation" paths (open ocean to open ocean, or coast to coast) and two cross-bay paths (open ocean to coast, or coast to open ocean). We also divide the boundary into six segments to better understand the spatial distribution of origin and escape events. Any number of boundary segments can be considered, each defining a unique origin and fate.

The basic idea is simple to describe. In our analysis domain, velocities from the HF radar measurements are objectively mapped to 4982 regularly spaced grid points (see Fig. 1b). The velocity archive we analyze here consists of roughly 62 days of hourly measurements

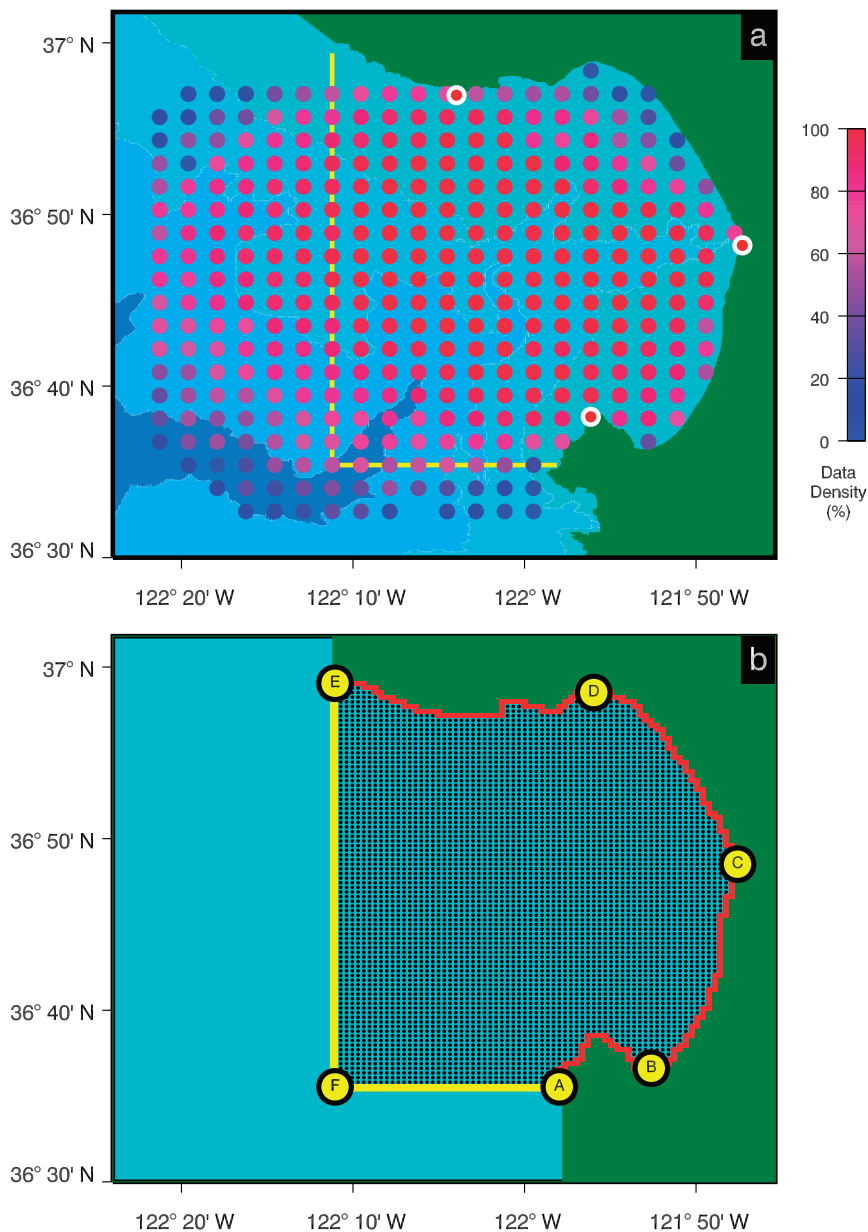


Figure 1. (a) Monterey Bay, with radar total velocity measurement locations color coded to show the percentage of time during the study period that a measurement was available at that location. The three radar sites are shown as red circles along the coastline. The 100-m, 1,000-m and 2,000-m isobaths are shown in blue. The objective mapping open boundary is also shown, in yellow. (b) The objective mapping and particle analysis grid. The center of each mapping grid cell is shown as a black dot. The coastal encounter zone (one-half km wide) is shown in red. The open ocean encounter zone (also one-half km wide) is shown in yellow. Five reference points A-F are also shown around the boundary.

Table 1. Types of SLMs

Type	Time direction	Boundary segments	Type of information shown	Information shown	Number of possible values	Shown in these figures
<i>If</i>	Forward	2	Spatio-temporal	Forward residence time Fate location	Any 2	3e-h, 7a, 7d
<i>Ib</i>	Backward	2	Spatio-temporal	Backward residence time Origin location	Any 2	3a-d
<i>IIf</i>	Forward	6	Spatial	Escape location along boundary	6	9a-d
<i>IbB</i>	Backward	6	Spatial	Origin location along boundary	6	9e-h
<i>III</i>	Both	N/A	Temporal	Total residence time	Any	3i-l
<i>IV</i>	Both	2	Spatial	Transport pathway	4	3m-p

on this grid, corresponding to 7,413,216 velocities. Since the velocity field is unsteady and not periodic (the non-stationarity described above), at each time the velocity at a given position gives rise to a unique particle trajectory, which extends both backward and forward in time. Hence, our Eulerian velocity archive contains 7,413,216 (Lagrangian) particle trajectories. How can we possibly make sense of all this information?

Rather than facing the “information overload” that comes from considering the location of every particle at each observation time, we choose to compress the analysis problem for each particle by considering only its origin/fate and its residence time inside the domain. We represent each trajectory as a single pixel that can be color-coded to show its residence time and/or information about its origin/fate. Our 62 day archive of 7,413,216 trajectories can now be represented as a sequence of hourly SLMs, each containing 4982 color-coded pixels, with one pixel per trajectory. Since a typical trajectory often consists of roughly 1000 positions when a ten-minute integration step is used, SLMs serve as a novel *data compression* tool for revealing Lagrangian transport structure and information by reducing trajectories to pixels.

Table 1 shows the types of SLMs that we present here, including references to the figure numbers where each type is shown. Types *If* and *IIf* use information from the forward time integration only. Types *Ib* and *IbB* use information from only the backward time integration. Types *III* and *IV* combine information from integration in both time directions. Note that for type *If* and *Ib* SLMs, space and time information for each particle are encoded in a single pixel using a dual color palette scheme.

b. Forward time integration: Particle fates

Many practical transport problems focus on the evolution of small patches of ocean surface that become significant due to events like oil spills or harmful algal blooms. In these cases, tracking both the residence time and escape fate for all particles inside the patch becomes more important than the details of individual trajectories as they move through the domain. A single type *If* SLM, summarizing 4982 trajectories on the analysis grid, gives this information at a glance. Patches can be overlaid on the SLM to determine

the range of residence times and escape fates for the patch. In addition, the influence of position uncertainty can be addressed by examining the SLM structure in the vicinity of the patch location.

As mentioned above, the type *If* SLM is reminiscent of the notion of an “escape time” from a domain that is studied in dynamical systems theory (see Meiss, 1997 for a nice review of this topic). However, there are two points of departure. One is that the dynamical systems approach has only been applied to *stationary dynamics*, i.e., flows that are either constant or periodic in time. Our flow fields are non-stationary, i.e., they are not periodic in time. The second point is that we are considering more than just the question of “escape from a domain.” We are considering how the particle escapes (if it escapes at all). The number of different possible fates will be application dependent.

c. Backward time integration: Particle origins

The trajectories used to create a single SLM reveal many different surface transport pathways and allow their relative importance to be assessed. A pathway is defined by the location of a particle’s entry to and exit from the domain. While the notion of particle escape has been examined in other dynamical systems studies, less attention has been paid to particle entry into a domain (origin). Integrating backward in time identifies particle origins, and the combined information from the forward and backward time integrations can be used to group particles into one of four possible transport pathways. The type *IV* SLM shows the spatial distribution of particles following each of these four paths.

Part of the analysis domain boundary joins the open ocean, providing an obvious source for particles originating along this open boundary segment. Flow into the domain from the coastal zone is an equally plausible but less obvious source of particles. Particle sources in a coastal zone cell (one-half km by one-half km, see Fig. 1b) include: receding tides, river and freshwater runoff, precipitation in excess of evaporation, and alongshore or vertical flow into the cell.

d. Computation of SLMs

Particles are initialized at every radar measurement time (hourly) at the center of each mapping grid cell. The particle positions are then integrated forward or backward in time, using an adaptive Adams-Gear scheme with a ten minute integration time step. Velocities for the integration are interpolated from the mapped velocity archive using bicubic interpolation in space and a third order Lagrange polynomial for interpolation in time (Mancho *et al.*, 2006). Each particle is tracked until it enters either the coast or open ocean encounter zone (each is one-half km wide). The time and location of each particle’s entry into an encounter zone is then used to compute total residence time and origin/escape classification. The mapping grid and the coast and open ocean encounter zones are shown in Figure 1b, with the 4982 particle initial positions (mapping cell grid centers) shown as black circles.

Specification of finite-width open-ocean/coast-encounter zones is an important aspect of residence time calculations. These zones eliminate regions where: (1) there are no radar observations; (2) the currents are strongly influenced by the coastline shape and by bottom topography; and (3) the surf zone currents vary on time and space scales much smaller than those resolved by radar observations in the bay's interior. Moreover, these zones eliminate numerical difficulties that often arise when tracking particles very close to a domain boundary, when the integration scheme may require velocities from outside the domain (on land, or offshore of the open boundary), producing numerical errors. Here, a ten-minute integration step combined with one-half km zone widths ensured that no particles jumped across the open ocean/coastal zones during one integration step. Selected SLMs computed using two km open ocean/coastal zone widths differed only in small-scale details from those discussed here.

During this analysis period, a typical particle remained inside the bay for about seven days, producing a record of roughly 1000 ten-minute positions. Our 62-day analysis produced 4982 trajectory pairs (forward and backward time), each containing roughly 1000 positions, every hour for 1488 hours. The result is more than seven billion positions, a significant computational burden.

3. HF radar measurements of surface currents

Hourly surface currents in Monterey Bay were measured continuously from 2000 UT, 2 June 1999 through 0200 UT, 4 August 1999 by a network of three CODAR-type HF radars. Surface velocities were inferred from the measured Doppler shift of the Bragg scattering lines, using the method described in Barrick *et al.* (1977) and Paduan and Graber (1997). The measurements were averaged over one-hour intervals, and total surface velocities were reported on a grid with a uniform spacing of 2.5 km. Figure 1a shows Monterey Bay and the radar total velocity grid used during the study period. Each measurement grid location is color coded to show the percentage of the analysis period during which measurements were available. Figure 1b shows the particle analysis grid. Figure 2a shows a time series of the total number of radar measurements available for each hour of the study period. Figure 2b shows a time series of the maximum distance from any mapping grid point to the nearest radar measurement. This distance, an estimate of the largest spatial gap in the data footprint at any time, is useful for determining the maximum spatial resolution that can be used for objective mapping (see Appendix).

Paduan and Rosenfeld (1996) made quantitative comparisons between CODAR-type HF radar measurements and ADCP measurements near the center of Monterey Bay, reporting rms speed differences of 6-11 cm s^{-1} and rms direction differences of about 51° . Chapman *et al.* (1997) compared phased array (not CODAR-type) HF radar surface current measurements with simultaneous ADCP measurements off Cape Hatteras and concluded that radar radial velocities agreed with the ADCP measurements to about 7-8 cm s^{-1} . The same results were reported by Shay *et al.* (1998) over a range of currents of 100 cm s^{-1} . Paduan *et al.* (2001) reported rms differences of 11-13 cm s^{-1} between CODAR-type HF radar (with measured rather than ideal antenna patterns) and ADCP

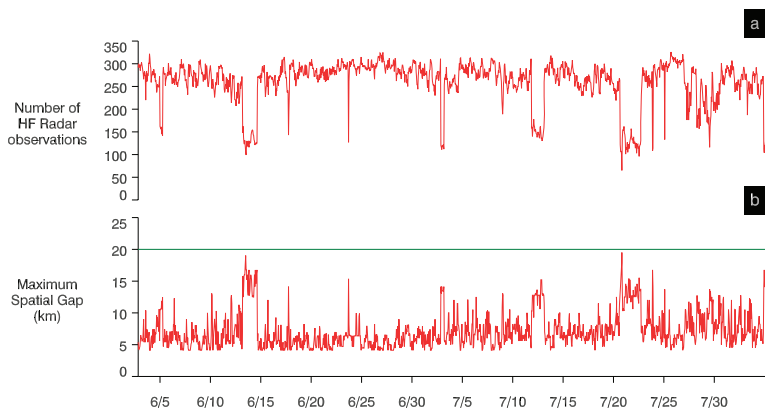


Figure 2. Time series of (a) the number of radar measurements available and (b) the maximum distance (in km) from any analysis grid point to the nearest radar measurement (a measure of spatial gap size), for each hour. The maximum allowed spatial gap size of 20 km is shown as a green line in (b).

measurements just outside the Chesapeake Bay mouth. Determining the precise accuracy of radar measurements is difficult, however, since the radar measures electromagnetic scattering from surface waves, while other sensors (like ADCPs or current meters) measure properties in the first few meters of the water column. In addition, the HF radar measurement time (hours) and space ($7\text{-}8\text{ km}^2$) scales are much larger than those for other sensors, which report measurements every few minutes over scales of a few square meters.

CODAR-type HF radars do not give a complete archive of synoptic maps because the spatial coverage varies with time, time gaps in the measurements occur occasionally, and there are often no measurements near the coastline or along the baselines between radar sites. Since particle trajectory calculations require a gap-free synoptic velocity archive, objective mapping is used to fill space and time gaps, enforce no-normal flow at the coastline, and match the radar-measured normal flow at the open boundaries. The method used here, normal mode analysis (NMA), has been used by Eremeev *et al.* (1992) to study the Black Sea circulation and by Lipphardt *et al.* (2000) to blend HF radar measurements with model velocities in Monterey Bay. Similar objective mapping methods have also been applied to Lake Ontario (Rao and Schwab, 1981), the Texas-Louisiana shelf (Cho *et al.*, 1998), and Monterey Bay (Chu *et al.*, 2003; Lekien *et al.*, 2004). The Appendix provides a description of the objective mapping procedure.

4. Results

Here we apply the analysis and data described in Sections 2 and 3 to Monterey Bay. This is the largest of thirteen US national marine sanctuaries and supports an extremely diverse and productive ecosystem. The bay's surface currents respond energetically to omnipresent diurnal and semidiurnal tide and sea breeze oscillations (Foster, 1993; Petrucio *et al.*,

1998). Surface currents also rapidly respond to lower-frequency forcing, most notably wind fluctuations between upwelling-favorable (toward the southeast) and relaxation (toward the northeast) conditions, often seen during the summer (Breaker and Broenkow, 1994; Rosenfeld *et al.*, 1994; Paduan and Rosenfeld, 1996; Ramp *et al.*, 2005). At longer timescales Paduan and Rosenfeld (1996) have also shown that the surface currents respond to mesoscale interactions of the bay with the California Current.

Hourly Monterey Bay surface currents, objectively mapped from HF radar measurements, were available for the period 2000 UT, 2 June 1999 through 0200 UT, 4 August 1999. Using this velocity archive, the fate of more than 99.9% of particles on the analysis grid could be determined for the period 2300 UT, 2 June 1999 through 0500 UT, 27 July 1999. The origin of more than 99.9% of these particles could be determined for the period 0700 UT, 14 June 1999 through 0000 UT, 4 August 1999. The origin or fate of a very small percentage of the longest-lived particles might be undetermined due to the finite nature of the velocity archive.

Even with the simplest division of the analysis boundary into two segments (open ocean and coastal regions), type *Ib* (*If*) SLMs showing particle origin (fate) and time in the bay since entry (until escape) reveal a rich spatio-temporal structure of surface transport. This structure could not be detected or anticipated from any Eulerian representation of the surface velocity field. Hourly maps during the study period show complex spatial structures at scales from 2 km (the radar resolution) to 40 km (the width of the bay mouth). These structures evolve rapidly over one day, reflecting the energetic influence of the diurnal wind and tide fluctuations. Most particles enter the bay along the boundaries with the open ocean, although near the coastline, narrow bands of particles originating from the coastal zone are almost always present. Type *Ib* and *If* SLMs often contain bands or filaments that are a few km wide. At times, groups of the longest-lived particles evolve into tightly spiraled filament structures with spatial scales as small as 5-10 km. Figure 3 shows four example SLM sets at seven-day intervals for 0000 UT during the period 17 June through 8 July 1999. Figure 3 (a-d) shows weekly examples of type *Ib* SLMs, with each particle shown as a colored pixel representing both the particle's origin location (blue hues show particles originating from the open ocean and red hues show particles originating from the coastal zone) and its time in the bay since entry. The brightness of each hue is proportional to the particle's time since entry, as shown by the dual color palette below this figure group. Figure 3 (e-h) shows weekly type *If* SLMs. Using the same dual palette color scheme (shown below these figures), red particles will encounter the coastline, while blue particles will escape to the open ocean. Particle brightness is proportional to the particle's remaining time in the bay. These example particle origin and fate maps are typical for this period. Most particles enter from the open ocean, although near the coastline there are bands of particles entering from the coastal zone. These example maps show that the spatial distributions of particle origin/fate can be quite complex and change markedly over a one-week period. A number of small-scale structures are evident, including long thin filaments (Fig. 3 a,c,h), narrow channels, (Fig. 3 d,f,g) and small circular spirals (Fig. 3 e,f). In Figure 3(a,b,i,j,m,n), particles with undetermined origin are shown as yellow pixels.

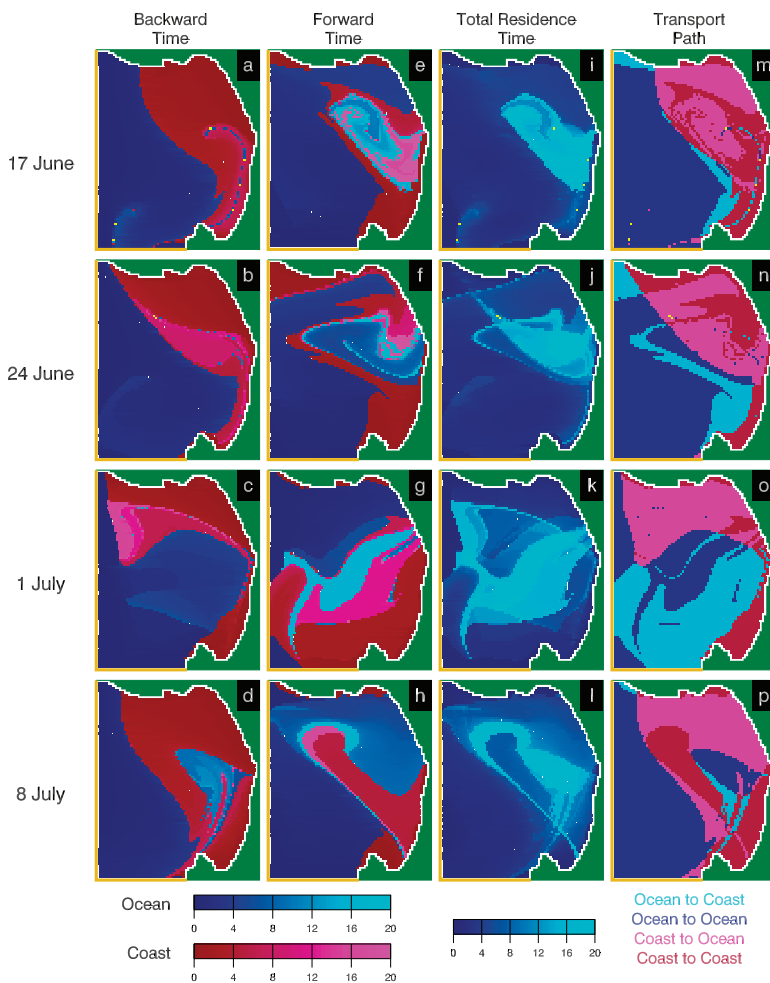


Figure 3. Type *Ib* SLMs (a-d); type *If* SLMs (e-h); type *III* SLMs (i-l); and type *IV* SLMs (m-p) for 0000 UT at weekly intervals during the analysis period. Particles with undetermined origin (due to the length of the velocity record) are shown as yellow pixels. Residence times are in days. Animated maps are at <http://newark.cms.udel.edu/~brucel/slmaps>.

Figure 3 (i-l) shows type *III* SLMs of total particle residence time using the blue hued color palette shown below this column. The structure shown in the type *Ib* and *If* maps is evident in these maps, with the long filament structures made up of particles with the longest residence times. Figure 3 (m-p) shows type *IV* SLMs, which classify particles by transport pathway. Four colors are used to represent each of four possible transport pathways, as noted below this column of figures. The two blue hues correspond to particles originating from the open ocean, while the two red hues show particles entering from the coastal zone.

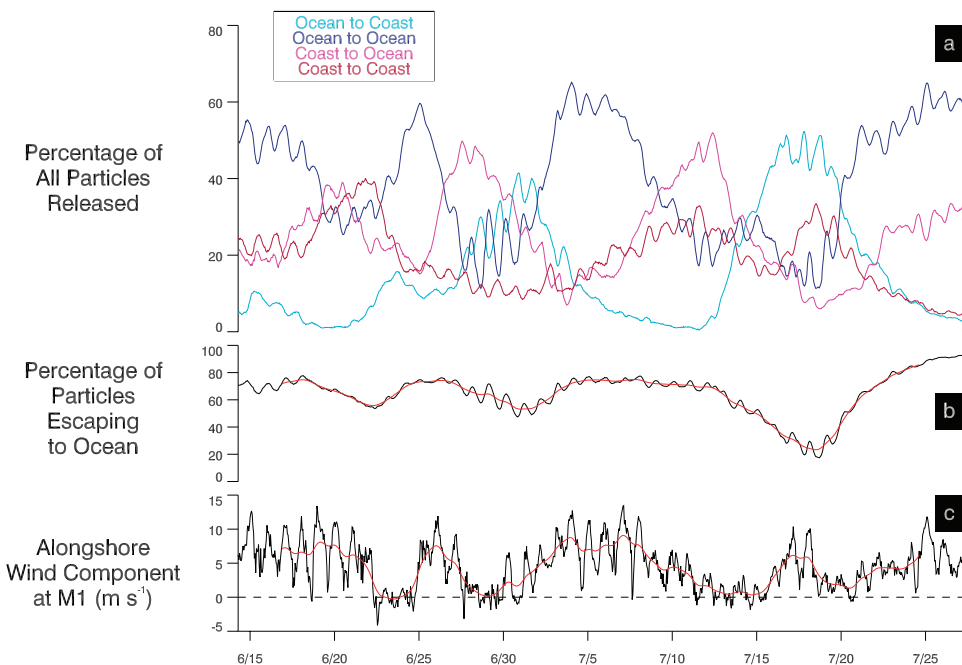


Figure 4. Time series of (a) the fraction of particles following one of four transport pathways through Monterey Bay; (b) the fraction of particles that escapes to the open ocean (black) and the 40-hour low-pass filtered version of this time series (red); (c) The hourly time series (black) and the 40-hour low-pass filtered time series (red) of the wind component at MBARI buoy M1 parallel to the bay mouth (alongshore). Positive (negative) alongshore wind blows toward a direction of 120° (300°). Buoy M1 is located near the center of the bay (see Fig. A4 for its location).

Figure 4a shows a time series of the fraction of particles following each of the four transport pathways shown in the maps in Figure 3 (m-p). Figure 4b shows a time series of the fraction of particles that escapes to the open ocean (black) and the 40-hour low-pass filtered version of this time series (red). The hourly time series (black) and the 40-hour low-pass filtered time series (red) of the wind component at MBARI buoy M1 parallel to the bay mouth (alongshore) are shown in Figure 4c. Positive (negative) alongshore wind blows toward a direction of 120° (300°). Buoy M1 is located near the center of the bay (see Fig. A4 for its location).

Diurnal fluctuations related to the combined effects of winds and tides are evident in Figure 4 (a,b). Lower frequency fluctuations in Figure 4 (a,b) may be related to low-frequency wind fluctuations seen in Figure 4c, although the relationship is not very clear. The fraction of particles escaping to the open ocean (Fig. 4b) varies from about 17% to more than 92% over the analysis period. Since the wind is likely to be one important factor that influences the fraction of particles escaping to the open ocean, we computed the Spearman rank correlation between the two 40-hour low-pass filtered time series in

Figures 4b and 4c. This correlation is 0.52, with a significance value of zero, indicating that the correlation is significant. Some lead/lag relationship between these time series may also exist, but this is not explored here. While this correlation result is suggestive, it should be interpreted with caution, since the wind time series represents an instantaneous point measurement while the particle fraction time series represents a quantity integrated over many particle trajectories that span a period several days into the future. We interpret the Spearman rank correlation result as indicating that the wind is one important forcing mechanism, but this result is hardly sufficient to quantify a cause and effect relationship.

Figure 5 shows histograms of total residence time for three particle populations: all particles, particles that escape to the open ocean, and particles that encounter the coast. The bulk distributions for the entire 62 day trajectory archive (Fig. 5a, 5f, and 5k) are broad and somewhat irregular. Four samples from this archive, corresponding to the analysis times for the type III SLMs shown in Figure 3(i-l), show markedly more variability and indicate that the bulk distributions are not reliable proxies for the hourly maps. All of the histograms in Figure 5 have long narrow tails with some total residence times greater than twenty days. Mean total residence time values for the populations shown in Figure 5 range from 4.9 days to 11.0 days.

For each hour, a mean total residence time is computed from the backward and forward time trajectories for all particles launched at that hour. Figure 6 shows a time series of mean total residence time for all particles (Fig. 6a), particles that escape to the open ocean (Fig. 6b) and particles that encounter the coast (Fig. 6c). A diurnal signal is evident in all of these time series. The mean total residence time for all particles (Fig. 6a) ranged from 4.5 to 11.0 days. These values are comparable to earlier estimates of two to twelve days (with mean values of about six days) for the north and south bay inferred from salinity, temperature, and nutrient tracer observations obtained from hydrographic cruises (Broenkow and Smethie, 1978). However, given the variability of the total residence time distributions shown in Figure 5, these mean residence time statistics must be used with caution.

Studies of evolving fluid patches reveal the underlying complexity of particle trajectories and the spatial distribution of escape locations. Figure 7 compares the evolution of two fluid patches, one which remains coherent for its entire time in the bay (Fig. 7 a-c), and one which undergoes rapid deformation and stretching (Fig. 7 d-f). Each of these patches is initially circular, with a diameter of four km, and consists of 3000 simulated particles. In Figure 7, particles are colored to show their residence time and escape fate according to the dual color bars shown at the bottom. Figures 7a and 7d show each patch initial position overlaid as a white circle on the type II SLM for the patch initialization time. The locations of all escape cells into which at least one particle escapes are shown in red around the domain boundary in Figures 7c and 7f.

The patch shown in Figure 7 (a-c) was initialized at 0000 UT, 17 July 1999 and remains coherent in the bay for slightly more than one week, ultimately exiting through a very narrow strip of coastline on the west side of the Monterey peninsula. Particle positions on

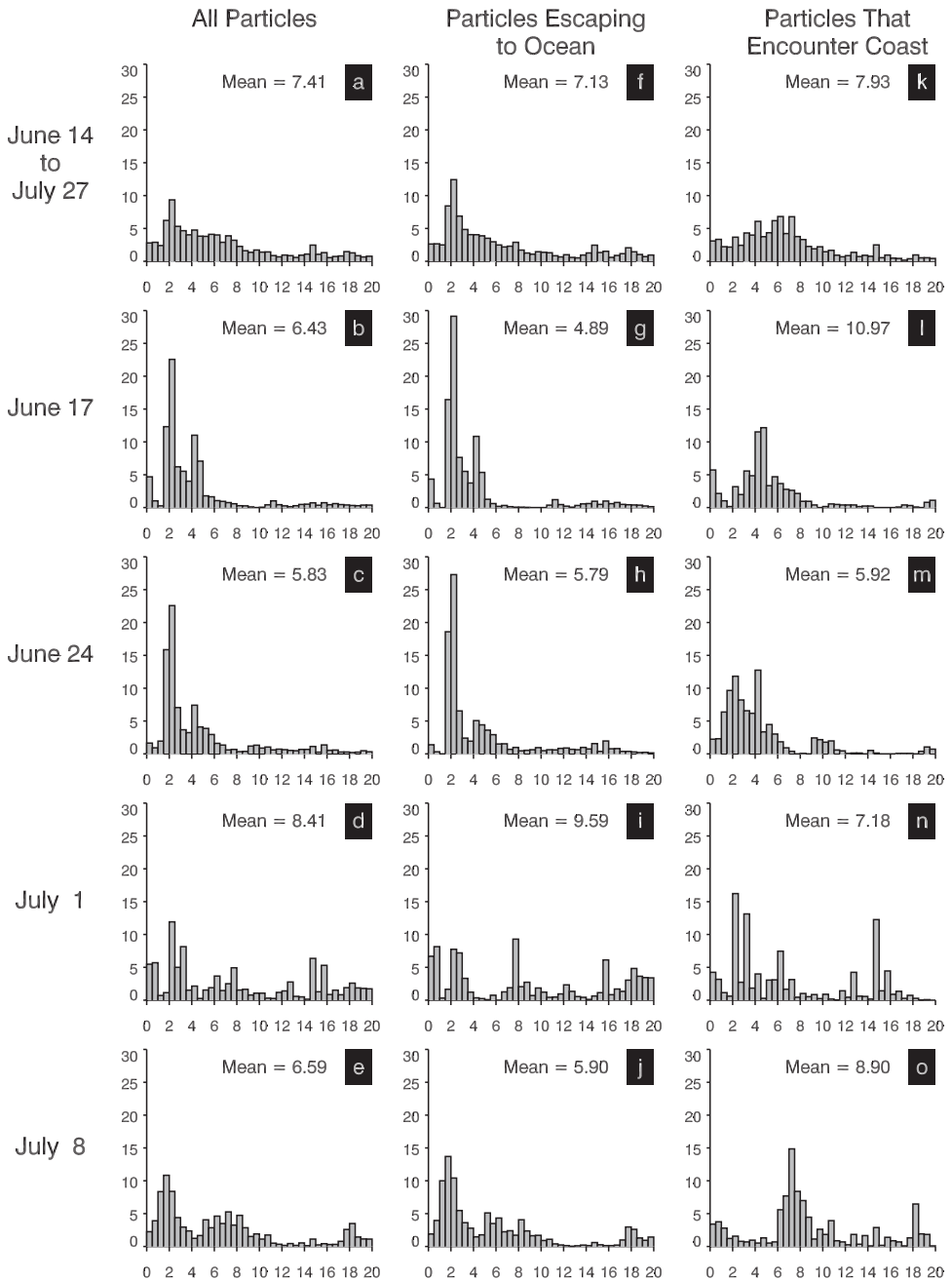


Figure 5. Histograms showing the distribution of total residence times (in days) for all particles (a-e); particles escaping to the open ocean (f-j); and particles encountering the coast (k-o). The x-axis values are in days, and the y-axis values are in percent of all particles in the group. The mean values of the group are also shown above each histogram.

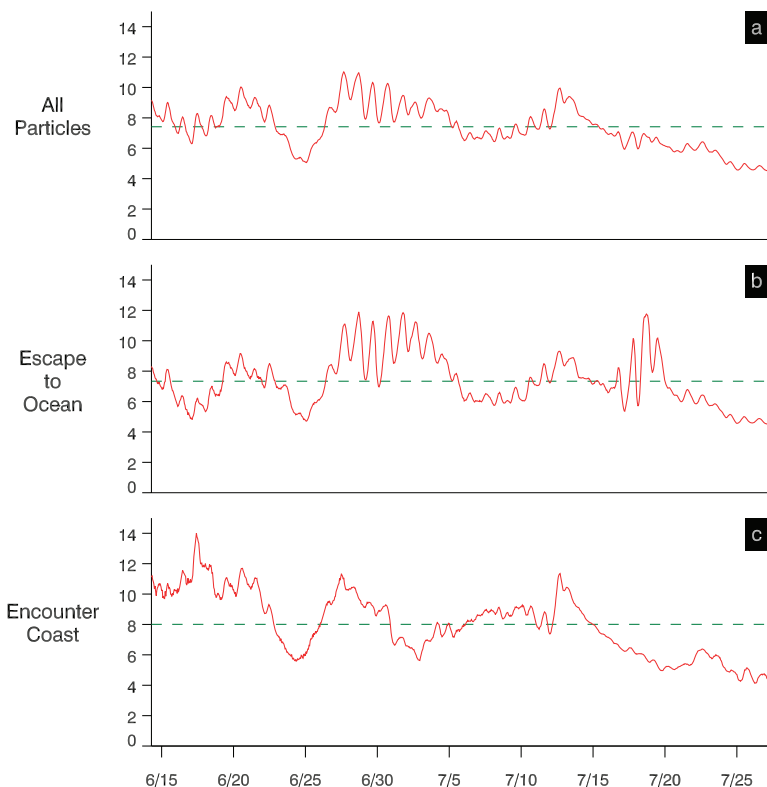


Figure 6. Time series of mean total residence time (in days) for (a) all particles; (b) particles that escape to the open ocean; (c) particles that encounter the coast. The mean value for each time series is shown as a dashed green line.

21 July (Fig. 7b) show that the patch retains its coherent structure while moving around the center of the bay. Some convergence is evident as the patch's area shrinks. The patch shown in Figure 7 (d-f) was initialized at 0000 UT, 21 June 1999 and undergoes rapid deformation and stretching. The patch's initial position encompasses both particles which escape to the open ocean and those reaching the coast (Fig. 7d). After fourteen days, the patch has undergone quite a bit of stretching (Fig. 7e). After 21 days, the patch extends across most of the lower bay, and particles will soon begin reaching the coast along the northern half of the inner bay. The red boundary cells highlighted in Figure 7f show that particles from this patch reach long segments along the inner bay coastline and the western and southern open boundaries. This extent of contact with the domain boundary contrasts sharply with the patch shown in Figure 7 (a-c), which exited entirely through one small coastline segment on the Monterey peninsula.

While dividing the domain boundary into two segments (open ocean and coastline) reveals a number of complex particle spatial distributions (see Fig. 3), trajectory results

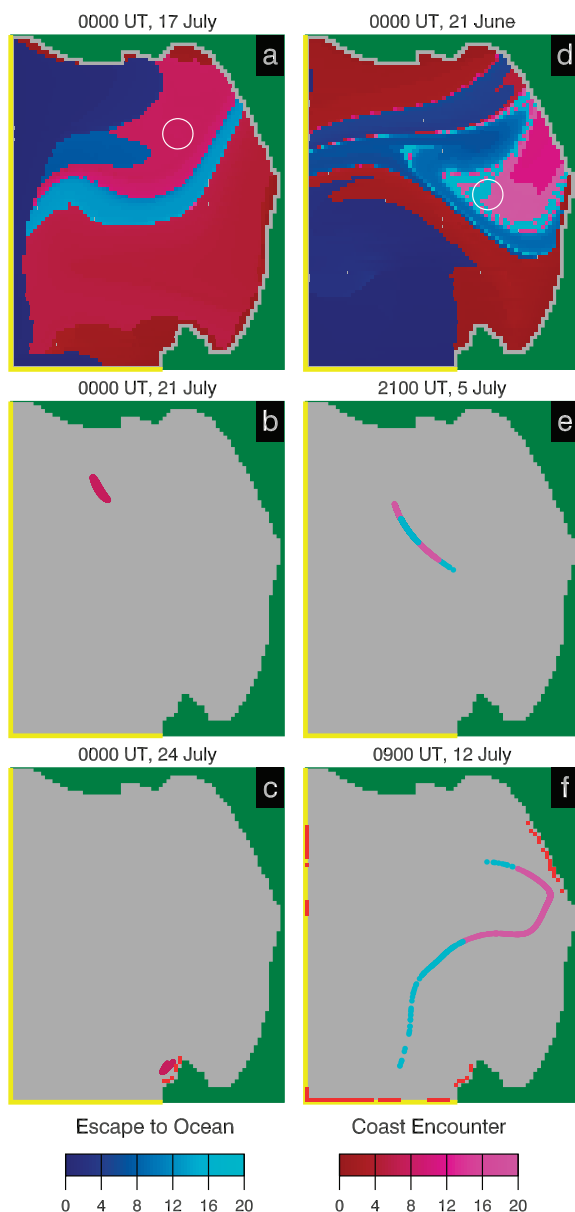


Figure 7. The evolution of a circular patch which remains coherent (a-c) compared with that of a patch undergoing strong deformation and stretching (d-f). Each patch is initially four km in diameter and contains 3000 particles. The type *If* SLMs for these two initial conditions are shown in (a) and (d). Residence times are in days. See text for discussion. Animations of these evolving patches can be viewed at <http://newark.cms.udel.edu/~bruce/slmaps>.

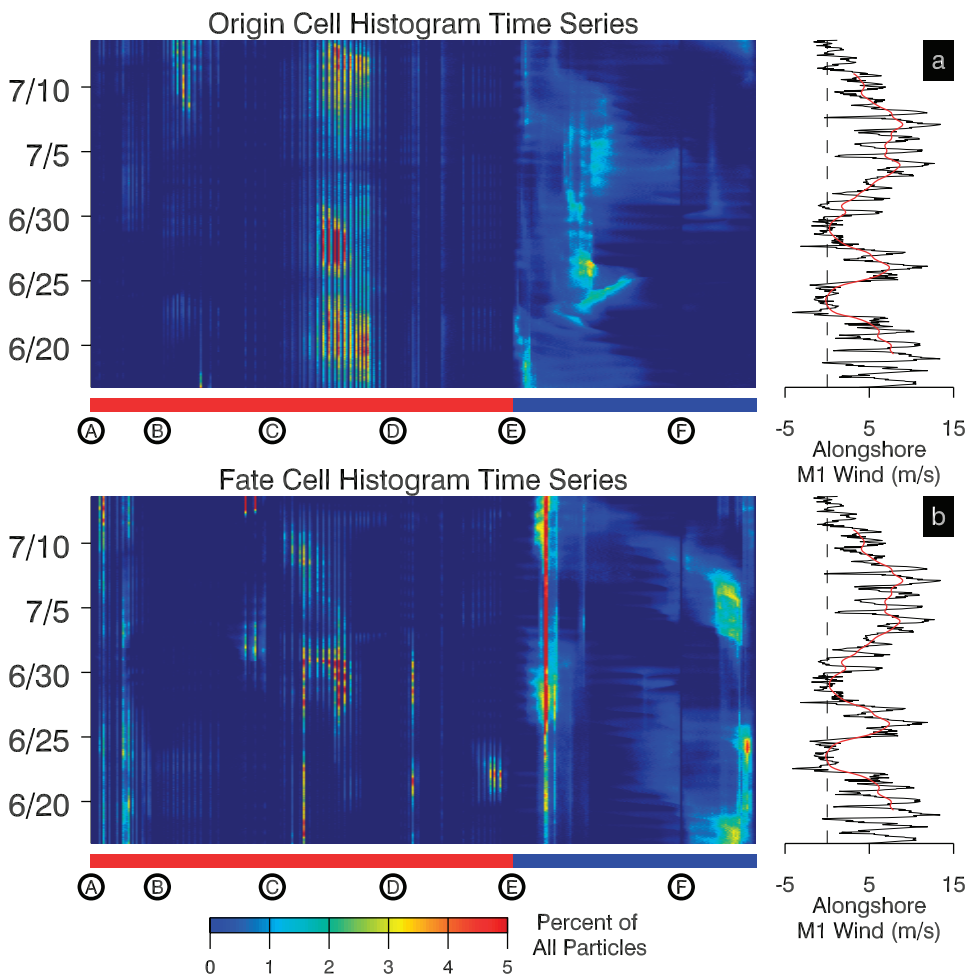


Figure 8. Time series of histograms showing the along-boundary distribution of particle origins and fates along the analysis domain boundary. The x axis shows the entire domain boundary, stretched out as a line, with boundary reference positions A-F as shown in Figure 1. Each boundary grid cell represents one histogram bin. Time increases along the y axis. For each hour, the histograms show the distribution of origins and fates for all particles initialized at analysis grid cell centers at that hour. The origin and escape events summarized by the histograms therefore occur at many different times. The hourly time series (black) and the 40-hour low-pass filtered time series (red) of the wind component at MBARI buoy M1 parallel to the bay mouth (alongshore) is shown at the right. Positive (negative) alongshore wind blows toward a direction of 120° (210°).

like those shown in Figure 7 motivated us to examine the distribution of particles entering and exiting the domain more closely. Figure 8 shows time series of histograms of the along-boundary distribution of particle entry and exit events for particles located at each grid cell center at the histogram reference time. Each of 342 boundary cells are stretched

out in a right-handed sense along the x axis, with the origin corresponding to reference point A where the open boundary meets the southern peninsula (see Fig. 1b). Boundary reference points A-F (shown in Fig. 1b) are labeled along the x axis. Each boundary cell is one-half km wide and corresponds to one histogram bin. Time proceeds along the positive y axis. At each hour, particles initially located at each grid cell center are tracked both backward and forward in time, and their entry and exit boundary cell are determined. The total numbers of these particles entering from or exiting into each boundary cell are then shown as histograms referenced to the initialization time along the y axis in Figure 8 (a-b). Note that since individual particle residence times vary, these entry and exit events occur at many different times. The alongshore component of the wind at MBARI buoy M1 (as shown in Fig. 4c) is also shown at the right.

The origin cell histograms in Figure 8a show three events (centered roughly around June 21, June 28, and July 11), each lasting 3-5 days and characterized by a large fraction of particles originating along the coastline between points C and D. These three events might be associated with three periods of strong alongshore winds (40-hour low-pass filtered values greater than 5 m s^{-1}) that roughly correspond with them in time, although the phasing is not precise. A correlation between the alongshore wind and the fraction of particles originating from the coastline segment between points C and D, if it exists, is plausible, since it is consistent with Ekman surface layer dynamics. Strong, persistent alongshore winds will tend to drive surface flow directed out of the bay (to the right of the wind). Under these conditions, one might expect more particles to originate near the coastline. Since we cannot track particles closer than one-half km from the coast and their motion is restricted to be purely horizontal, we have no way of assessing whether upwelling might also occur.

One of the most notable surface current responses to wind relaxations in Monterey Bay during summer is the rapid reversal of flow along the southern open boundary of our analysis domain (segment between boundary points F and A in Fig. 1b). Periods of strong alongshore winds drive a strong southerly flow along this open boundary. When the wind veers toward the east-northeast (a relaxation event) the surface currents along this open boundary segment quickly shifts to predominant northerly flow (see Ramp *et al.*, 2005, for example). If surface winds are an important forcing mechanism for transport, a decrease in the fraction of particles escaping along the southern open boundary in response to a wind relaxation event would be expected. Evidence for this relationship between alongshore wind and particle escapes along the southern open boundary is not apparent in the fate cell histograms shown in Figure 8b. The low-pass filtered wind record shown at the right in Figure 8b shows two relaxation events (when the alongshore wind approaches zero) centered roughly on June 24 and June 29. The fate cell histograms immediately following the June 24 relaxation event show a large fraction of particles exiting along the southern open boundary. The fate cell histograms immediately following the June 29 relaxation event show a sharp decrease in the fraction of particles exiting to the south. These results are inconclusive. While the alongshore wind may influence transport along the southern

open boundary, it is clear that other factors, such as the phasing of wind events with the tides and/or offshore flow features, cannot be ignored.

When the boundary is divided into six segments, the distribution of particle origin/fate can be more precisely mapped, as shown in the type *Iib* and *IIf* SLMs in Figure 9. Boundary reference points A through F show the endpoints for each boundary segment, and each segment is color-coded as shown in each panel. Most particles enter the bay either through the western open boundary (between points E and F) or along the northeast segment of the inner bay coastline (between points C and D), consistent with the histograms shown in Figure 8a. The particle fate maps (Fig. 9 e-h) include more small-scale spatial structure than the origin maps (Fig. 9 a-d). When particles exit to the open ocean, they most often do so through the southern open boundary.

5. Discussion

We tracked a regular grid of 4982 particles both backward and forward in time to determine their origin and fate for each hour during a 62-day period in June-August 1999. This large collection of particle trajectories was then used to produce a variety of SLMs that summarize particle residence time, origin/fate, and transport pathway. Semi-diurnal and diurnal surface current fluctuations (due to the combined effects of winds and tides) are energetic throughout the bay, and the evolution of hourly SLMs reflects this variability. While the smallest Eulerian spatial scale included in our velocity maps was 20 km, many of the SLMs we computed (see Fig. 3 for example) show spatial variability ranging from 2 to 40 km, with long filaments no more than a few km wide often present. This is not surprising, however, since even a very large-scale diurnal oscillation with a magnitude of 20 cm s^{-1} can produce particle path fluctuations on scales of a few kilometers or less. The disparity between Eulerian and Lagrangian spatial scales in the ocean is well known (see for example Ridderinkhof and Loder, 1994).

The fraction of particles that escape to the ocean varies from about 17% to more than 92% during the analysis period (Fig. 4b). Although the mean total particle residence time (Fig. 6a) ranged from 4.5 to 11.0 days, the variability of total residence time distributions shown in Figure 5 illustrates that these mean values do not capture the character of residence time distributions for these trajectories.

We examined the relationship between alongshore wind (measured at a single point near the center of the bay) and: (1) the fraction of particles that escapes to the open ocean (Fig. 4) and (2) the distribution of particle origins and fates around the boundary (Fig. 8). We found a statistically significant Spearman rank correlation of 0.52 between the alongshore wind and the fraction of particles escaping to the open ocean. This suggests that, while synoptic scale alongshore wind may be one important forcing mechanism, the influence and phasing of tidal currents or offshore flow, as well as spatial variations in the wind field, must also be considered. Figure 8a shows some evidence that strong alongshore winds toward the southeast may drive an offshore surface flow that results in an increased fraction of particles originating near the coast, although the phasing of the wind and surface

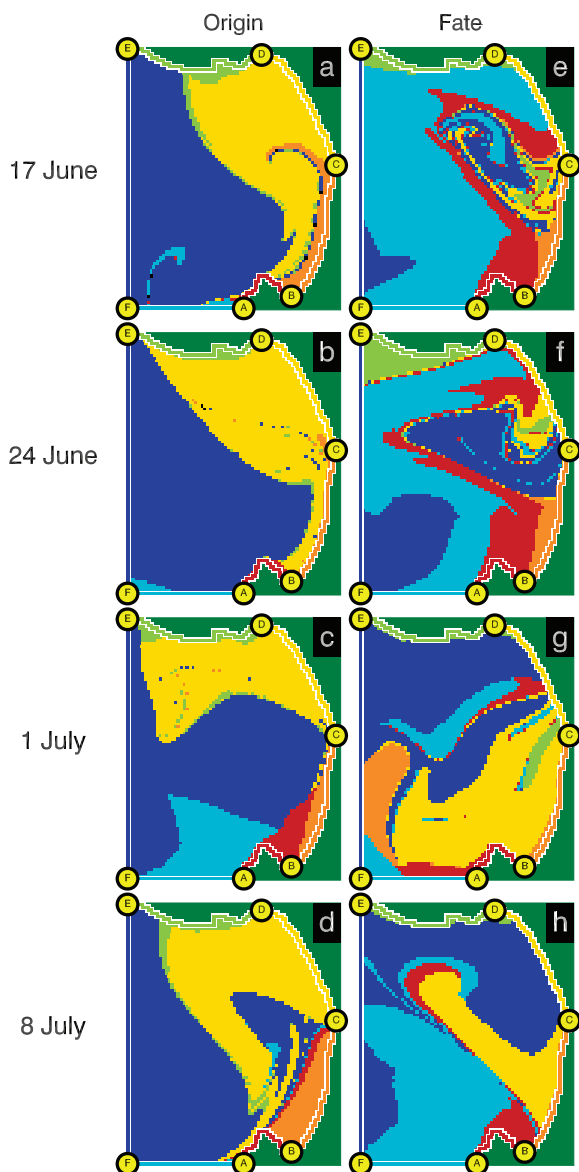


Figure 9. Type *IIIb* (a-d) and *IIIf* (e-h) SLMs at weekly intervals for the period 17 June through 8 July 1999. The boundary is divided into six segments, with segment boundaries marked by reference points A through F. The boundary segments are color coded as shown in each panel. Particles are colored to show the boundary segment that they originate from (a-d) or exit into (e-h). Particles which could not be tracked from entry through exit due to the length of the velocity record are shown in black. Animated maps are at <http://newark.cms.udel.edu/~brucel/slmaps>.

transport response is not clear. Figure 8b shows that, even though surface currents along the southern open boundary are known to rapidly reverse from south to north in response to a wind relaxation event, the influence of these current reversals on particle fates along the southern boundary is not obvious, so that other forcing mechanisms likely play an important role.

We also found great variability in the fates of particle patches. Information from the type *If* SLMs allowed us to initialize two patches with markedly different fates. The patch illustrated in Figure 7 (d-f) quickly filamented with most particles ultimately exiting over most of the bay mouth. In contrast, another patch (Fig. 7 a-c) remained coherent over a seven-day period and exited the bay along a narrow segment of the Monterey peninsula.

For non-stationary flows like the Monterey Bay currents studied here, the synoptic particle behavior described by an SLM cannot be readily discerned while browsing an Eulerian velocity archive. Also, when semi-diurnal and diurnal fluctuations are energetic, particle trajectories cannot be reliably predicted in any sense by examining low-pass filtered or averaged Eulerian fields. Perturbation velocities are not small when compared with the mean. This should serve as a strong caution for coastal oceanographers attempting to assess transport using only Eulerian data. The compressed Lagrangian information in the evolving SLMs provides an additional method for assessing models of coastal ocean circulation.

This Lagrangian analysis found substantial variability in surface particle transport properties in Monterey Bay. It is reasonable to question whether this is an artifact of the analysis and not a fundamental property of the HF radar surface current measurements. While HF radar provides oceanographers with unprecedented high-resolution synoptic maps of surface currents, the resolution and nature of the measurements prevent precise benchmarking with other sensors. In this situation we have to accept the radar data as the best available representation of nature. We recognize that HF radar measurements include uncertainties arising both from the measurement technique and from unresolved processes at space scales below the radar resolution. Does Lagrangian analysis like that performed here distort the current measurements? The answer is unequivocally no. The analysis merely advects particles based on interpolations from the observed synoptic velocity archive and introduces no additional uncertainty. Will unresolved processes influence particle trajectories? The answer is certainly yes. Since neither the measurements nor the effects of unresolved processes can be reliably benchmarked, the robustness of our results would best be tested with a carefully designed deployment of real drifters. These results suggest that the distribution of residence times from an ensemble of real drifter trajectories would likely be highly variable.

This analysis documents the wide range of time and space scales over which surface particle properties can vary in Monterey Bay. At least three energetic forcing mechanisms drive the surface flow: semi-diurnal and diurnal tides, wind fluctuations at both diurnal time scales and at 2-10 day event scales, and forcing at the open boundary due to mesoscale fluctuations in the California Current system further offshore. Our analysis shows a clear

relationship between the alongshore wind measured at a single point near the center of the bay and the distribution of particle origins along the boundary. Some influence of alongshore wind on the distribution of particle fates along the boundary is also evident. While tidal currents and mesoscale variability along the open boundary also influence the evolution of particle trajectories, we cannot readily partition the radar surface velocities to isolate the surface currents contributions from these forcing mechanisms. Detailed measurements of the ocean mass field, if available, would certainly permit a more thorough dynamical treatment of radar velocities. Note that the influence of semi-diurnal and diurnal winds and tides is apparent in every particle property we have studied, so that low-pass filtered or de-tided analyses or simulations will fail to capture an energetic part of the surface transport picture.

These results have implications for environmental risk assessment. The range of variability in the fates of the two particle patches shown here (Fig. 6) suggests that narrow coastline segments may be at high risk in the event of a pollutant release or harmful algal bloom, depending on the location and time of the event. While type *If* SLMs cannot be used as a predictive tool for real-time problems (since they require information for as much as twenty days or more into the future) cautious use of historical velocity archives may provide some insight about the range of particle behaviors one might expect in a particular region.

Acknowledgments. Financial support by the Royal Society, the Mary A. S. Lighthipe endowment, and the U.S. Office of Naval Research is gratefully acknowledged.

APPENDIX

Objective mapping using NMA

The NMA technique (Lipphardt *et al.*, 2000) projects the radar measurements onto two sets of geometric orthogonal functions (GOF) each capturing distinct physical processes that are important in Monterey Bay. The vorticity modes describe the variability of coherent structures like eddies and jets. The horizontal divergence modes are associated with tidal and sea breeze responses. In Monterey Bay, both GOF sets contain energetic motions at semi-diurnal and diurnal scales. Both GOF sets have no normal flow at all boundaries. A separate boundary solution matches the observed normal flow along the open boundaries. Mappings that include both GOF sets represent an important extension of prior work where divergence effects were assumed to be negligible (Rao and Schwab, 1981; Cho *et al.*, 1998).

The GOF sets used for an NMA mapping do not depend on the measurements and do not vary with time. Their structure depends only on the geometry and resolution of the mapping domain and they are ordered by increasing spatial resolution. The mapping grid (4982 total grid cells) is uniform, with one-half km spacing in both the east-west and north-south directions (Fig. 1b). The mapping grid open boundary was positioned to encompass the center of the radar footprint (where the measurements are most plentiful and

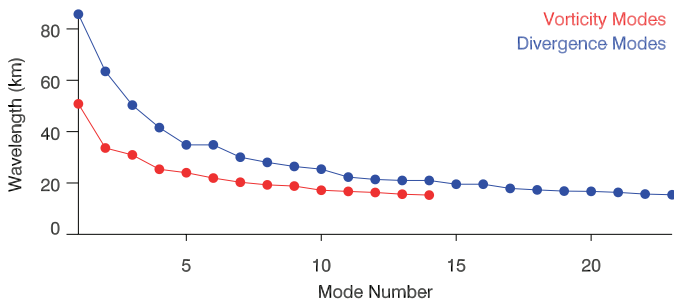


Figure A1. Mode wavelength versus mode number for all GOFs with wavelengths greater than 15 km. The set consists of the first 14 vorticity modes (red) and the first 23 horizontal divergence modes (blue). The minimum wavelength used for the mappings described here (20 km) is shown as a horizontal line.

accurate) while maximizing the open boundary normal flow information available from the radar measurements. This open boundary also serves as a natural demarcation between the bay and its offshore environment. See Figure 1.

The NMA method relies on a numerical Poisson solution to account for specified normal flow through the open boundaries (Lipphardt *et al.*, 2000). As shown in Figure 1a, radar measurements were available along most of the open boundary segments at least 60% of the time during the study period. Along these boundaries, time gaps in the radar measurements were filled using tidal harmonic fits and these radar measurements were interpolated onto the higher resolution mapping grid boundary using an along-open-boundary bicubic spline with zero normal velocity where the open boundaries meet the coast. The open boundary normal flow condition for the Poisson problem is specified from the interpolated radar measurements. Other approaches (Chu *et al.*, 2003; Lekien *et al.*, 2004) have been developed to infer open boundary flow from interior measurements when no open boundary velocity measurements are available. The Poisson solution form used here (which decays rapidly when moving from the boundary toward the interior) ensures that the effects of uncertainties in the specified open boundary normal flow will remain localized near the open boundary. We tested this by rotating some open boundary normal flows by 180 degrees. The resulting differences in the boundary solution were confined to local regions within five km of the boundary segments where the boundary normal velocities were rotated.

As with any spectral method, some objective criterion must be used to select the (spatial) GOF modes used, setting the mapping's spatial resolution. Lipphardt *et al.* (2000) elected to retain all GOFs that had a mean kinetic energy that was at least 15% of the most energetic GOF. Recently, Chu *et al.* (2003) described a technique similar to NMA which used a mode set satisfying homogeneous mixed open boundary conditions. This mode set is time-dependent and thus permits time-dependent spatial resolution in the mappings.

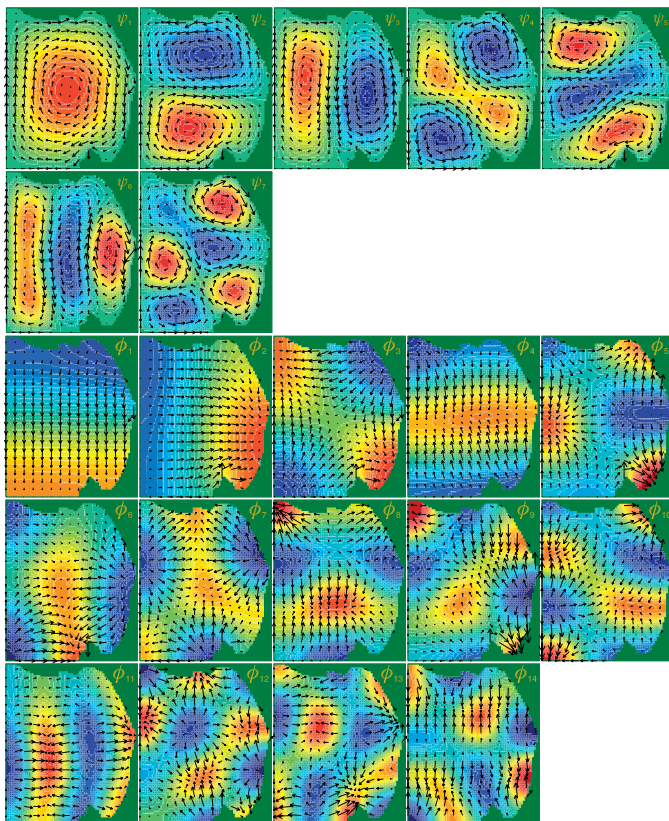


Figure A2. The seven vorticity modes (ψ_1 through ψ_7 , top two rows) and the fourteen horizontal divergence modes (ϕ_1 through ϕ_{14} , bottom three rows) used for the objective mappings described here. The color contour interval is nondimensional, with lower values in blue and higher values in red, and nondimensional velocity vectors are overlaid in each panel.

Since we cannot predict how time-varying spatial resolution in a velocity archive might affect computed particle trajectories, we chose instead a minimum mode wavelength of 20 km, applied separately to both the vorticity and divergence modes. This minimum mode wavelength criterion ensures that: (a) there are at least eight radar measurements- (spaced 2.5 km apart) per mode wavelength (a conservative requirement), and (b) no GOF mode can introduce aliasing or false spatial structure across any spatial gap, since the largest spatial gap in the velocity archive is less than 20 km (Fig. 2b).

Applying the 20 km minimum mode wavelength criterion yielded 21 total GOF modes: the first seven vorticity modes plus the first fourteen horizontal divergence modes. Figure A1 shows the wavelength L ($L = 2\pi/\lambda$, with λ defined as the eigenvalue of the Helmholtz eigenvalue problem for a domain with an irregular boundary, in units of km) for all GOFs with wavelengths greater than 15 km. Figure A2 shows the spatial structure of the 21 GOF modes

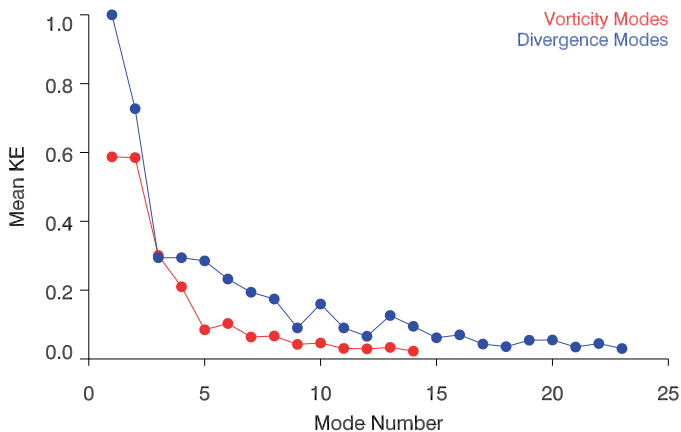


Figure A3. The kinetic energy (scaled by the largest mode energy) for vorticity modes 1-14 (red) and divergence modes 1-23 (blue), integrated over the study period.

used here. Since the measurements are projected onto the GOFs using simple least squares, and there are typically at least 300 velocity component measurements to constrain each NMA map, the mappings are always strongly constrained (overdetermined).

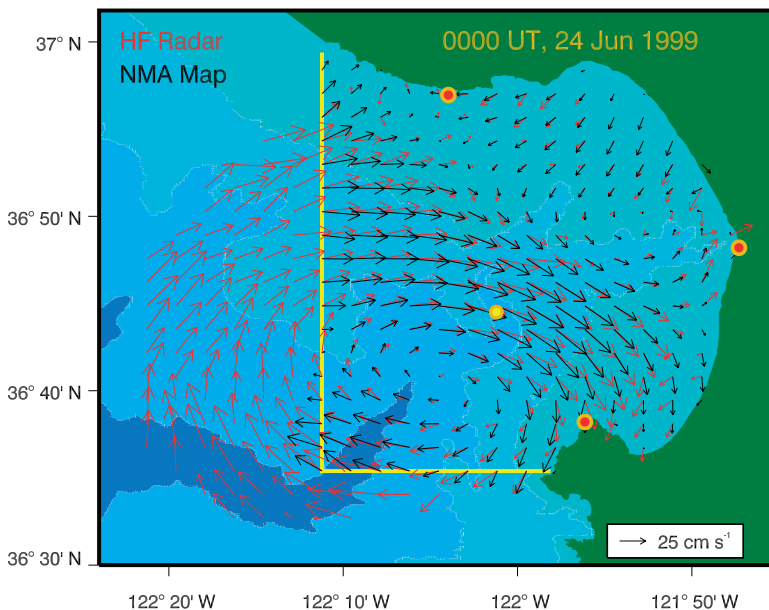


Figure A4. Radar measured (red vectors) and mapped (black vectors) surface currents in Monterey Bay for 0000 UT, 24 June 1999. The location of Monterey Bay Aquarium Research Institute mooring M1 is shown in yellow near the center of the bay.

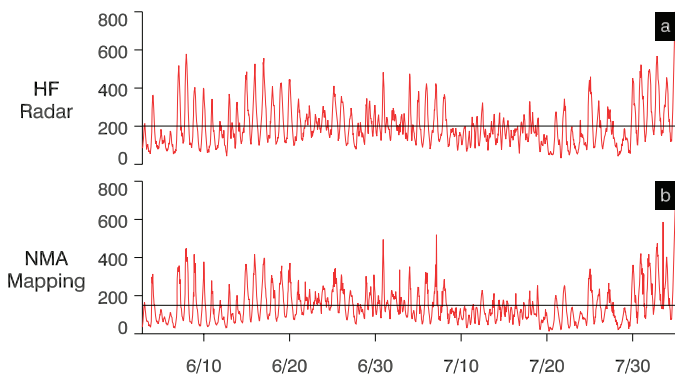


Figure A5. Time series of mean kinetic energy (in $\text{cm}^2 \text{s}^{-2}$) for (a) All radar measurements and (b) mapped velocities at the same locations. On average, the mapping accounted for 74.4% of the mean measured kinetic energy. The correlation between the two time series is 0.95 after the mean of each time series is removed.

We have studied mappings that retain higher GOF modes. For example, Figure A3 shows the kinetic energy (scaled by the largest mode energy) for all modes with wavelengths greater than 15 km (the 14 vorticity modes and 23 horizontal divergence modes shown in Figure A1) integrated over the study period. All of the discarded vorticity modes (vorticity modes 8 and higher and divergence modes 15 and higher) have less than 10% of the maximum mode kinetic energy.

Examination of the 21 NMA mode amplitude time series showed that the radar measurements, as expected, contained some high-frequency noise. We elected to minimize the influence of this noise on the mapping by low-pass filtering each mode amplitude time series using a Butterworth filter with an eight-hour cutoff period. The filter window was steep enough so that the semi-diurnal (12 hour) band was not affected.

An example of the radar measured (red vectors) and the mapped (black vectors) surface currents for 0000 UT, 24 June 1999 is shown in Figure A4. A time series of the mean kinetic energy for all radar measurements is shown in Figure A5a. Figure A5b shows a time series of the mean mapped kinetic energy at the same locations. On average, the mappings accounted for more than 74% of the mean measured kinetic energy. The correlation between the two time series shown in Figure 7 is 0.95 after the mean of each time series is removed.

REFERENCES

- Allen, J. S., R. C. Beardsley, J. O. Blanton, W. C. Boicourt, L. K. Coachman, A. Huyer, T. H. Kinder, T. C. Roger, J. D. Schumacher, R. L. Smith, W. Sturges and C. D. Winant. 1983. Physical oceanography of continental shelves. *Rev. Geophys. Space Phys.*, 21, 1149-1181.
- Barrick, D. E., M. W. Evans and B. L. Weber. 1977. Ocean surface currents mapped by radar. *Science*, 198, 138-144.
- Breaker, L. C. and W. W. Broenkow. 1994. The circulation of Monterey Bay and related processes. *Oceanogr. Mar. Biol.*, 32, 1-64.

- Broenkow, W. W. and W. M. Smethie, Jr. 1978. Surface circulation and replacement of water in Monterey Bay. *Estuar. Coast. Mar. Sci.*, *6*, 583-603.
- Bryden, H. L., D. Halpern and R. D. Pillsbury. 1980. Importance of eddy heat flux in a heat budget for Oregon coastal waters. *J. Geophys. Res.*, *85*, 6649-6653.
- Camassa, R. and S. Wiggins. 1991. Chaotic advection in a Rayleigh-Bénard flow. *Phys. Rev. A.*, *43*, [774-797](#).
- Chapman, R. D., L. K. Shay, H. C. Graber, J. B. Edson, A. Karachintsev, C. L. Trump and D. B. Ross. 1997. On the accuracy of HF radar surface current measurements: Intercomparisons with ship-based sensors. *J. Geophys. Res.*, *102*, 18737-18748.
- Cho, K., R. O. Reid and W. D. Nowlin Jr. 1998. Objectively mapped stream function fields on the Texas-Louisiana shelf based on 32 months of moored current meter data. *J. Geophys. Res.*, *103*, 10,377-10,390.
- Chu, P. C., L. M. Ivanov, T. P. Korzhova, T. M. Margolina and O. V. Melnichenko. 2003. Analysis of sparse and noisy ocean current data using flow decomposition. Part 1: Theory. *J. Atmos. Ocean. Tech.*, *20*, 478-491.
- Cook, T. M. and L. K. Shay. 2002. Surface M_2 tidal currents along the North Carolina shelf observed with a high-frequency radar. *J. Geophys. Res.*, *107*, 3222, [doi:10.1029/2002JC001320](#).
- Csanady, G. T. 1982. *Circulation in the Coastal Ocean*. D. Reidel, Norwell, MA, 279 pp.
- Dever, E. P. 1997. Subtidal velocity correlation scales on the northern California shelf. *J. Geophys. Res.*, *102*, 8555-8571.
- Dever, E. P. and S. J. Lentz. 1994. Heat and salt balances over the northern California shelf in winter and spring. *J. Geophys. Res.*, *99*, 16,001-16,017.
- Eremeev, V. N., L. M. Ivanov and A. D. Kirwan Jr. 1992. [Reconstruction of oceanic flow characteristics from quasi-Lagrangian data, 1: Approach and mathematical methods](#). *J. Geophys. Res.*, *97*, 9733-9742.
- Foster, M. D. 1993. Evolution of diurnal surface winds and surface currents for Monterey Bay. M.S. thesis, Naval Postgrad. School, Monterey, CA, 100 pp.
- Hallock, Z. R., P. Pistek, J. W. Book, J. L. Miller, L. K. Shay and H. T. Perkins. 2002. A description of tides near the Chesapeake Bay entrance using *in situ* data with an adjoint model. *J. Geophys. Res.*, *108*, 3075, [doi:10.1029/2001JC000820](#).
- Lekien, F., C. Couillette, R. Bank and J. Marsden. 2004. Open-boundary modal analysis: Interpolation, extrapolation, and filtering. *J. Geophys. Res.*, *109*, [doi:10.1029/2004JC002323](#).
- Lentz, S. J. 1994. Current dynamics over the northern California inner shelf. *J. Phys. Oceanogr.*, *24*, [2461-2478](#).
- Lipphardt, B. L., Jr., A. D. Kirwan Jr., C. E. Grosch, J. K. Lewis and J. D. Paduan. 2000. Blending HF radar and model velocities in Monterey Bay through normal mode analysis. *J. Geophys. Res.*, *105*, 3425-3450.
- Mancho, A. M., D. Small and S. Wiggins. 2006. [A comparison of methods for interpolating chaotic flows from discrete velocity data](#). *Computers & Fluids*, *35*, 416-428.
- Meiss, J. D. 1997. Average exit time for volume preserving maps. *Chaos*, *7*, 139-147.
- Paduan, J. D., D. Barrick, D. Fernandez, Z. Hallock and C. Teague. 2001. Improving the accuracy of coastal HF radar current mapping. *Hydro International*, *5*, 26-29.
- Paduan, J. D. and H. C. Graber. 1997. Introduction to high-frequency radar: Reality and myth. *Oceanography*, *10*, 36-39.
- Paduan, J. D. and L. K. Rosenfeld. 1996. Remotely sensed surface currents in Monterey Bay from shore-based HF radar (Coastal Ocean Dynamics Application Radar). *J. Geophys. Res.*, *101*, 20,669-20,686.
- Petruncio, E. T., L. K. Rosenfeld and J. D. Paduan. 1998. [Observations of the internal tide in Monterey Canyon](#). *J. Phys. Oceanogr.*, *28*, 1873-1903.

- Ramp, S. R., J. D. Paduan, I. Shulman, J. Kindle, F. L. Bahr and F. Chavez. 2005. Observations of upwelling and relaxation events in the northern Monterey Bay during August 2000. *J. Geophys. Res.*, *110*, C07013, doi:10.1029/2004JC002538.
- Rao, D. B. and D. J. Schwab. 1981. [A method of objective analysis for currents in a lake with application to Lake Ontario. *J. Phys. Oceanogr.*, *11*, 739-750.](#)
- Ridderinkhof, H. and J. W. Loder. 1994. [Lagrangian characterization of circulation over submarine banks with application to the outer Gulf of Maine. *J. Phys. Oceanogr.*, *24*, 1184-1200.](#)
- Rom-Kedar, V., A. Leonard and S. Wiggins. 1990. [An analytical study of the transport, mixing, and chaos in an unsteady vortical flow. *J. Fluid Mech.*, *214*, 347-394.](#)
- Rosenfeld, L. K., F. B. Schwing, N. Garfield and D. E. Tracy. 1994. [Bifurcated flow from an upwelling center: A cold water source for Monterey Bay. *Cont. Shelf Res.*, *14*, 931-964.](#)
- Shay, L. K., S. J. Lentz, H. C. Graber, D. B. Ross and B. K. Haus. 1998. Current structure variations detected by high frequency radar and vector measuring current meters. *J. Atmos. Technol.*, *15*, 237-256.¹

Received: 21 September 2004; revised: 10 January 2006.